Journal of Electrical Engineering and Computer (JEECOM)
Vol. 8, No. 2 (2026), DOI: 10.33650/jeecom.v8i2.17123
p-ISSN: 2715-0410; e-ISSN: 2715-6427

Physics-Informed Deep Sequential Learning and Non-Parametric Adaptive Thresholding for Integrated Microgrid Fault Detection

Muhammad Akbar Barrinaya[1], Herminarto Nugroho [2*]
[1] Department of Mechanical Engineering, Faculty of Industrial Technology, Universitas Pertamina, Jakarta, Indonesia
[2] Department of Electrical Engineering, Faculty of Industrial Technology, Universitas Pertamina, Jakarta, Indonesia

Article Info

Article history:

Received August 26, 2026
Revised September 7, 2026
Accepted September 8, 2026

Keywords:

Fault Detection and Isolation
Integrated Microgrids
Solar Photovoltaic Systems
Deep Learning
Kernel Density Estimation

ABSTRACT

The rapid proliferation of clean energy microgrids—integrating solar photovoltaic (PV) generation, bidirectional power converters, and battery energy storage systems (BESS)—requires robust fault detection and isolation (FDI) to guarantee continuous operational stability. However, non-Gaussian residual profiles caused by severe irradiance intermittency and dynamic switching transients compromise traditional fixed-threshold strategies, resulting in elevated false alarm and missed detection rates. To address this challenge, this study presents a hybrid FDI framework combining physics-guided deep sequential forecasting with non-parametric adaptive thresholding. A Temporal Convolutional Network integrated with Long Short-Term Memory (TCN-LSTM), constrained by equivalent circuit and DC bus power balance equations, is developed to forecast multi-modal nominal trajectories and extract reliable diagnostic residuals. Raw electrical streams sampled at 10 kHz are down sampled via moving-window averaging to 10-second intervals to accommodate prognostic forecasting horizons. Non-parametric Kernel Density Estimation (KDE) is subsequently implemented to dynamically compute adaptive threshold boundaries from empirical non-Gaussian residual distributions. Simulation experiments under stochastic irradiance profiles and dynamic load cycles confirm that the proposed TCN-LSTM architecture achieves nominal forecasting RMSE values of 0.007 V for cell voltage and 0.306 °C for temperature, reducing the missed detection rate of PV shading mismatches and critical sensor biases compared to static thresholding. Furthermore, integration with a Local Outlier Factor (LOF) anomaly detector provides early warning margins of 83.5 minutes for micro-short circuit voltage dips and 24.6 minutes for thermal runaway precursors prior to hard-limit BMS alarms.

Corresponding Author:
Herminarto Nugroho,
Department of Electrical Engineering, Faculty of Industrial Technology, Universitas Pertamina, Jakarta, Indonesia
Email: herminarto.nugroho@universitaspertamina.ac.id ; Orchid ID: https://orcid.org/0000-0002-8539-7195

1. INTRODUCTION

The accelerating transition toward sustainable electrical networks has established integrated microgrids as fundamental structures for clean energy utilization [1]. Modern microgrids coordinate distributed energy resources, advanced power conversion topologies, and dynamic energy storage to maintain grid resilience and meet bidirectional load demands. Within these topologies, solar photovoltaic (PV) arrays serve as primary energy generators, coupled with bidirectional DC-DC converters and high-capacity Battery Energy Storage Systems (BESS). However, the strong closed-loop coupling across power electronic stages, coupled with fluctuating operating patterns and switching transients, introduces operational vulnerabilities that accelerate hardware degradation and increase susceptibility to sensor anomalies [2], [3].

In PV-BESS microgrids, localized component anomalies propagate dynamically across shared bus interconnections, impairing operational safety [4]. Specifically, PV arrays are vulnerable to Partial Shading Conditions (PSCs), cracked modules, and dust accumulation. Shading mismatches reverse-bias unshaded cells, inducing localized hotspots and multi-peaked Power-Voltage $(P-V)$ characteristics. In parallel, power converter units undergo continuous electrical and thermal stress, leading to DC-link capacitor aging, semiconductor degradation, and sensor measurement drift [5]. When converter current sensor biases (f_{Is}) or voltage sensor drifts (f_{Vs}) manifest, the closed-loop control system injects harmonic ripples into the common DC bus. This propagation alters the discharge profile of the BESS, accelerating solid electrolyte interphase (SEI) layer growth, increasing internal cell resistance, and potentially driving internal micro-short circuits (f_{MSC}) toward catastrophic thermal runaway [6]. Conversely, battery current fluctuations disrupt the terminal voltage balance, adversely affecting the Maximum Power Point Tracking (MPPT) converter dynamics [1]. Hence, reliable Fault Detection and Isolation (FDI) frameworks capable of capturing multi-stage fault propagation are essential [3].

Traditional FDI techniques are broadly grouped into model-based observers, signal processing algorithms, and data-driven artificial intelligence. Model-based observers (such as Extended Kalman Filters and Sliding-Mode Observers) rely on first-principles governing equations; however, their performance deteriorates in the presence of unmodeled plant non-linearities and parameter drift [8], [9]. Signal-based methods (including Wavelet and Fourier transforms) process signature frequency deviations, but display limited reliability during transient microgrid load switching [7], [8], [9]. Purely data-driven architectures (such as CNNs and recurrent networks) map non-linear relations without explicit mathematical formulations, yet they operate as uninterpretable models that require extensive run-to-failure training data and lack physical compliance under out-of-distribution conditions [10].

To mitigate these limitations, hybrid frameworks combining physical priors with deep sequential networks have emerged. Nonetheless, a critical research gap persists in multi-source clean energy microgrids: under dynamic load variations and irregular solar irradiance, nominal residuals deviate sharply from standard Gaussian distributions, displaying multimodal, skewed, and heavy-tailed profiles [8], [9]. Conventional static (fixed) thresholds must be designed with excessively wide boundaries to avoid false alarms during rapid operational transients, which severely degrades residual sensitivity to early-stage sensor drift and incipient micro-short circuits. While non-parametric Kernel Density Estimation (KDE) has been applied in isolated electrical systems, its combination with physics-constrained temporal predictors for integrated PV-converter-BESS microgrids remains insufficiently developed. [8].

Therefore, the objective of this study is to formulate, implement, and validate a unified hybrid FDI and early warning framework capable of decoupling simultaneous cross-domain faults under non-Gaussian operational regimes. The technical contributions of this work are threefold:

1. Formulation of a physics-guided deep sequential forecasting network combining a Temporal Convolutional Network and Long Short-Term Memory (TCN-LSTM) constrained by equivalent circuit and DC bus power balance priors for robust nominal trajectory prediction.
2. Development of a non-parametric KDE adaptive thresholding mechanism that dynamically adjusts detection boundaries according to the empirical statistical variance of residuals, eliminating transient false alarms while maintaining sensitivity to subtle sensor and electrical faults.
3. Synthesis of an unsupervised Local Outlier Factor (LOF) anomaly prognostics pipeline that delivers quantifiable early safety margins ahead of conventional Battery Management System (BMS) hard-limit alarms.

The remainder of this paper is organized as follows: Section 2 discusses about methods which shows the high-fidelity mathematical and physical models of the coupled microgrid components, and details the formulation of the hybrid TCN-LSTM sequential predictor and the KDE-based adaptive threshold synthesis; Section 3 validates the diagnostic accuracy, noise resilience, and real-time response of the framework via high-fidelity co-simulations; and Section 4 concludes the study.

2. METHOD

2.1. Mathematical Modeling of Integrated Microgrid Physical Components

2.1.1. Solar Photovoltaic (PV) Generation Subsystem under Dynamic Shading

The electrical behavior of the PV modules is modeled using the highly precise double-diode equivalent circuit representation, which provides superior accuracy in capturing carrier recombination losses in the space charge region compared to the standard single-diode model [11], [12].

The output current I_{pv_out} of a single PV cell under varying junction temperatures and solar irradiance is formulated as

$$I_{pv\_out} = I_{ph} - I_{01}\left[\exp\left(\frac{V_{pv_{cell}}+I_{pv_{out}}R_S}{a_1V_t}\right)-1\right] - I_{02}\left[\exp\left(\frac{V_{pv+cell}+I_{pv_{out}}R_S}{a_2V_t}\right)-1\right] - \frac{V_{pv\_cell}+I_{pv\_out}R_S}{R_p} \quad (1)$$

where I_{ph} is the photo-generated current directly proportional to solar irradiance; I_{01} and I_{02} represent the reverse saturation currents of Diode-1 and Diode-2, respectively; a_1 and a_2 are the corresponding diode ideality factors; R_s and R_p represent the intrinsic series and parallel shunt resistances of the lamination sheets, characterizing internal ohmic losses and crystal defect leakage paths; $V_t = kT_j/q$ is the thermal voltage of the PN junction at temperature T_j.

For an extensive PV array consisting of N_s series-connected and N_p parallel-connected modules, the total output current I as a function of terminal voltage V is scaled as:

$$I = N_pI_{ph} - N_pI_{01}\left[\exp\left(\frac{\frac{V}{N_s}+\frac{IR_s}{N_p}}{a_1V_t}\right)-1\right] - N_pI_{02}\left[\exp\left(\frac{\frac{V}{N_s}+\frac{IR_s}{N_p}}{a_2V_t}\right)-1\right] - \frac{\frac{N_pV}{N_s}+IR_s}{R_p} \quad (2)$$

Under Partial Shading Conditions (PSCs), non-uniform solar irradiance causes mismatch losses among series-connected modules [13]. If a string contains shaded cells, their photo-generated current I_{ph} drops significantly. Consequently, the shaded cells become reverse-biased and act as loads rather than generators, consuming power and producing localized "hotspots" that can physically damage the panel [14]. To prevent this, bypass diodes are typically connected in parallel with strings [15]. This protection mechanism introduces multiple steps and local maxima in the Power-Voltage ($P - V$) curve, rendering conventional MPPT trackers (like Perturb & Observe) ineffective due to their tendency to get trapped in local Maximum Power Points (MPPs) [16], [17].

2.1.2. Boost Converter Dynamics and PSO-MPPT Optimization

To harvest maximum power under dynamic shading, the PV array is coupled with a DC-DC boost converter governed by a Particle Swarm Optimization (PSO)-based MPPT controller. The state-space averaged model of the boost converter operating in continuous conduction mode (CCM) is represented as

$$\frac{di_L}{dt} = \frac{V_{pv}}{L} - \frac{(1-D)V_{dc}}{L} \quad (3)$$

$$\frac{dV_{dc}}{dt} = \frac{(1-D)i_L}{C} - \frac{I_{out}}{C} \quad (4)$$

where i_L is the inductor current, V_{pv} is the PV array output voltage, V_{dc} is the DC microgrid bus voltage, D is the switching duty cycle, L is the filter inductance, and C is the output DC-link capacitor [18].

The PSO-MPPT algorithm dynamically optimizes the duty cycle D to track the Global Maximum Power Point (GMPP) under non-uniform shading. The velocity v and position (duty cycle) D_j of each particle j in the swarm are updated iteratively as

$$v_j(k+1) = wv_j(k) + c_1r_1\left(P_{best,j} - D_j(k)\right) + c_2r_2\left(G_{best} - D_j(k)\right) \quad (5)$$

$$D_j(k+1) = D_j(k) + v_j(k+1) \quad (6)$$

where w is the inertia weight, $c_1$and c_2 are cognitive and social acceleration coefficients, r_1 and r_2 are random variables uniformly distributed, $P_{best,j}$ is the individual best duty cycle recorded by particle j, and G_{best} is the global best duty cycle that maximizes the harvested PV power ($P_{pv} = V_{pv}I_{pv}$) across the entire swarm [1].

2.1.3. Battery Energy Storage System (BESS) Dynamics

The BESS serves as the dynamic buffer of the microgrid, stabilizing power fluctuations caused by intermittent solar generation and shifting load demands [19]. A single battery cell is represented using a high-fidelity equivalent circuit model (ECM) consisting of an open-circuit voltage source, an internal resistance, and parallel RC networks capturing polarization effects [20].

The terminal voltage of the battery pack is mathematically formulated as

$$V_{batt} = V_{oc} - I_{batt}R_i - V_p \quad (7)$$

where V_{oc} is the open-circuit voltage, which is a highly non-linear function of the State of Charge (SoC), I_{batt} is the charge/discharge current (defined as positive for discharge and negative for charge), R_i is the internal ohmic resistance of the cells, which degrades over time due to solid electrolyte interphase (SEI) buildup, V_p is the polarization voltage across parallel RC branches modeling transient electrochemical diffusion dynamics.

The temporal evolution of the State of Charge (SoC) is estimated recursively via Coulomb counting

$$SoC(t) = SoC(t_0) - \frac{\eta_c}{C_{nominal}} \int_{t_0}^{t} I_{batt}(\tau) d\tau \quad (8)$$

where $C_{nominal}$ is the nominal electrochemical capacity of the battery pack, and η_c represents the charging efficiency factor [21].

2.1.4. Microgrid Bus Integration and Coupled Fault Propagation

Within the integrated microgrid energy management system, the PV boost converter, BESS bidirectional buck-boost converter, and loads are linked via a shared DC bus [22]. Under nominal operation, the power balance at the DC bus must satisfy

$$P_{bus} = P_{pv} \pm P_{batt} - P_{load} = 0 \quad (9)$$

where P_{pv} is the power generated by the PV array, P_{batt} is the battery charging/discharging power, and P_{load} represents the microgrid's operational and load demand. In an EV-integrated microgrid, the dynamic motor load power is modeled as

$$P_{load} = P_{EV} = V_{batt} I_{batt} \eta_{inv} \eta_{motor} \quad (10)$$

where η_{inv} and η_{motor} represent the conversion efficiencies of the three-phase inverter and traction motor.

This shared physical connection establishes a strong bidirectional coupling. If a partial shading fault (f_{PSC}) occurs in the PV array, the MPPT converter's output drops suddenly, causing a power mismatch on the DC bus. To maintain bus voltage stability, the battery controller must quickly increase the discharge current (I_{batt}). This rapid rate of discharge increases the thermal stress on the battery pack [23].

Conversely, if a current sensor bias (f_{IS}) or a localized high-resistance connection fault occurs in the battery pack, it distorts the battery terminal voltage estimation (V_{batt}). This distortion compromises the closed-loop buck-boost control, generating voltage ripples that propagate back to the PV array DC-link capacitor. This cross-domain propagation can disrupt the PSO-MPPT tracking cycle and destabilize the microgrid. Modeling these coupled dynamics under a unified, system-level state space is therefore essential for isolating overlapping and simultaneous clean energy anomalies [24].

2.2. Physics-Guided TCN-LSTM Predictor and KDE Adaptive Thresholding

2.2.1. Network Architecture and Physics-Guided Constraint Mechanism

To generate residuals that are highly sensitive to incipient component anomalies and resilient to background switching noise, the nominal predictor must capture both multi-scale local features and long-term global dependencies hidden within the dynamic microgrid sensor streams [10]. Standard recurrent models (e.g., vanilla RNNs or LSTMs) struggle with computational bottlenecks and gradient degradation when processing high-frequency switching sequences [25]. Conversely, conventional convolutional networks (e.g., CNNs) lack the sequential causal constraints required to model long-term electrochemical and thermal degradation paths. To resolve these limitations, this framework integrates the parallel feature-extraction speed of a TCN with the robust temporal memory of an LSTM [26].

Physics-Guided Formulation: Unlike purely unconstrained black-box models, the input feature space is constructed using physics-informed invariants derived from equation (1)–(10). Specifically, alongside raw sensor signals, the theoretical nominal current $I_{pv,nominal}$ calculated from equation (2) and the target bus balance $P^*_{bus} = P_{pv} - P_{load}$ are integrated into the network input tensor. Furthermore, predictions are constrained during backpropagation by adding a physics-consistency penalty term to the Mean Squared Error (MSE) loss function:

$$\mathcal{L}_{total} = \mathcal{L}_{MSE}(y, \hat{y}) + \lambda_{phy} \| \hat{V}_{batt} - \left(V_{oc}\left(\widehat{SoC}\right) - \hat{I}_{batt} R_i - \hat{V}_p \right) \|_2^2 \quad (11)$$

Input Standardization and Sliding Window Processing

Prior to model training, raw multivariate mechatronic sensor measurements—comprising PV terminal voltages, boost converter currents, battery pack temperatures, and DC bus voltage levels—are normalized to eliminate dimensional scale discrepancies and improve gradient convergence [4], [27]

$$x_i^*(t) = \frac{x_i(t) - \mu_i}{\sigma_i} \quad (12)$$

where $x_i(t)$ represents the raw measurement of the i-th sensor at time t, and μ_i and σ_i are the corresponding mean and standard deviation estimated under nominal, fault-free historical operations.

The standardized time-series variables are subsequently processed using a sliding time window (TW) mechanism [28]. For an input matrix $X \in \mathbb{R}^{T \times N}$ representing N variables over T time steps, the sliding window extracts chronological segments of a fixed length t_{TW}

$$X(t) = \left[x^*_{t-t_{TW}+1}, x^*_{t-t_{TW}+2}, \cdots, x^*_t\right]^T \tag{13}$$

where $X(t)$ serves as the multi-dimensional temporal input tensor fed into the downstream network [29].

Temporal Convolutional Network (TCN) Feature Extraction

The normalized sequence tensor $X(t)$ is first processed by the TCN layer. The TCN architecture is constructed using a stack of residual blocks incorporating causal and dilated convolutions [30]. Causal convolutions ensure that the output at any time step depends strictly on past and current states, preventing future-data leakage during online forecasting [31]. To expand the model's receptive field without exponentially increasing the number of network parameters, dilated convolutions are employed. For a one-dimensional sequence $x \in \mathbb{R}^t$ and a convolution filter kernel $f = (f_0, f_1, \cdots, f_{m-1})$ of size m, the dilated causal convolution operation at step is mathematically formulated as

$$F(t) = (x *_d f)(t) = \sum_{i=0}^{m-1} f(i) x_{t-di} \tag{14}$$

where d is the dilation factor. In this study, the dilation factors are progressively scaled as $d \in \{1,2,4\}$ to capture multi-scale temporal abstractions across both high-frequency inverter switching and slow thermal trends.

To prevent gradient vanishing or exploding during multi-layer backpropagation, residual connections are implemented between TCN layers. The residual connection bypasses the convolutional blocks and performs an element-wise summation, formulated as

$$h_t^{(TCN)} = \text{Activation}\big(x(t) + F(t)\big) \tag{15}$$

where $x(t)$ is the input tensor, $F(t)$ is the output of the dilated causal convolution block, and the activation function is a Rectified Linear Unit (ReLU). The feature tensor $h_t^{(TCN)}$ is then passed through a linear projection layer to match the input dimensions of the subsequent LSTM layer [32], [33].

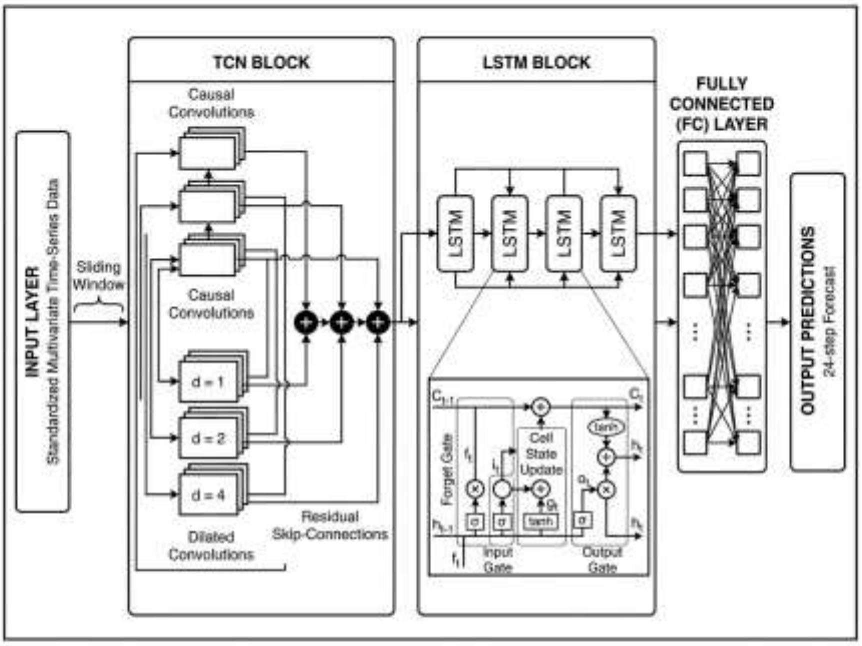

Figure 1. Schematic representation of the proposed hybrid TCN-LSTM network architecture.

LSTM Sequential Modeling and Residual Generation

The spatiotemporal features $h_t^{(TCN)}$ extracted by the TCN are forwarded to an LSTM network to track the global, long-term sequential dependencies of the microgrid [34], [35]. Inside each LSTM cell, three nonlinear gating units—the input gate (i_t), forget gate (f_t), and output gate (o_t)—regulate and protect the state evolution [36]

$$i_t = \sigma\big(W_i\big[z_{t-1}, h_t^{(TCN)}\big] + b_i\big) \tag{16}$$

$$f_t = \sigma\left(W_f\left[z_{t-1}, h_t^{(TCN)}\right] + b_f\right) \tag{17}$$

$$\widetilde{c_t} = \tanh\left(W_c\left[z_{t-1}, h_t^{(TCN)}\right] + b_c\right) \tag{18}$$

$$c_t = f_t \odot c_{t-1} + i_t \odot \widetilde{c_t} \tag{19}$$

$$o_t = \sigma\left(W_o\left[z_{t-1}, h_t^{(TCN)}\right] + b_o\right) \tag{20}$$

$$z_t = o_t \odot \tanh(c_t) \tag{21}$$

where σ represents the logistic sigmoid function, $\odot$ denotes element-wise vector multiplication, and W and b represent the respective weight matrices and bias vectors of each gate. The concatenated vector $\left[z_{t-1}, h_t^{(TCN)}\right]$ merges the hidden state z_{t-1} from the previous step with the TCN-derived local feature vector $h_t^{(TCN)}$.

Finally, the hidden state z_t is mapped to the target prediction space through a fully connected linear layer to output the forecasted nominal trajectory $\hat{y}(t)$

$$\hat{y}(t) = W_y z_t + b_y \tag{22}$$

Using the predicted nominal state, the multi-dimensional residual vector $r(t)$ is computed in real-time as the algebraic difference between the actual sensor measurements $y(t)$ and the predicted nominal output $\hat{y}(t)$

$$r(t) = y(t) - \hat{y}(t) \tag{23}$$

2.2.2. Statistical Analysis of Non-Gaussian Residuals

In complex, multi-source mechatronic environments like solar-integrated microgrids, healthy residual signals do not conform to standard normal distributions. Highly dynamic solar irradiance changes, partial shading transitions, and load fluctuations introduce unmodeled parameter variations, sensor noise, and mode-switching disturbances [8].

As a result, statistical analysis of healthy microgrid residuals reveals highly skewed, multi-modal, and long-tailed probability density profiles [37]. If a traditional fixed-threshold approach is applied under these conditions, the decision boundaries must be set conservatively wide to avoid triggering false alarms during transient power spikes [38]. However, these wide boundaries render the diagnostic system blind to subtle, early-stage anomalies—such as current sensor drifts or high-resistance contact failures—leading to high Missed Detection Rates (MDR). This trade-off necessitates a non-parametric, adaptive evaluation strategy.

2.2.3. Non-Parametric Kernel Density Estimation (KDE) and Adaptive Thresholding

To overcome the sensitivity bottlenecks of static boundaries, the proposed framework implements a non-parametric Kernel Density Estimation (KDE) strategy to model the empirical probability distribution of healthy residuals directly from online streaming data [39], [40]. KDE does not rely on restrictive parametric assumptions, enabling accurate density mapping of skewed and non-Gaussian signals [41], [42].

Given a training set of n healthy, fault-free residual samples $\{r_1, r_2, \cdots, r_n\}$ obtained during the offline calibration phase, the continuous empirical probability density function $\hat{f}(r)$ is formulated as

$$\hat{f}(r) = \frac{1}{nh}\sum_{j=1}^{n} K\left(\frac{r - r_j}{h}\right) \tag{24}$$

where h is the smoothing bandwidth parameter, and $K(\,.\,)$ is the standard Gaussian kernel function, represented as

$$K(u) = \frac{1}{\sqrt{2\pi}} \exp\left(-\frac{u^2}{2}\right) \tag{25}$$

Once the empirical probability density function is successfully constructed, the corresponding cumulative distribution function (CDF) is calculated to establish statistical confidence intervals. At a specified confidence level $1 - \alpha$ (where $\alpha = 0.05$ represents a 95% confidence level), the upper limit (r_u) and lower limit (r_l) of the healthy residual variation are determined as

$$P(r \le r_l) = \frac{\alpha}{2}, \quad P(r \le r_u) = 1 - \frac{\alpha}{2} \tag{26}$$

To account for dynamic operational transitions, these static limits are extended into dynamically adaptive threshold boundaries. By scaling the threshold limits with the magnitude of the real-time residual signal, the boundaries expand during aggressive transient maneuvers (e.g., sudden load shedding or cloud transients) and contract during steady-state operations. The dynamic upper threshold (Th^+) and lower threshold (Th^-) are synthesized as

$$Th^+ = r_i + (r_u - \mu)|r_i| \tag{27}$$

$$Th^- = r_i + (\mu - r_l)|r_i| \tag{28}$$

where μ is the statistical mean of the healthy calibration residuals, and r_i represents the real-time residual value under evaluation.

The real-time fault detection decision is governed by the following binary logic

$$\text{Decision} = \begin{cases} \text{Healthy (Free of Fault)}, & \text{if } Th^- \leq r_i \leq Th^+ \\ \text{Fault Occurs}, & \text{if } r_i > Th^+ \text{ or } r_i < Th^- \end{cases} \tag{29}$$

By implementing this KDE-based adaptive thresholding scheme, the FDI framework achieves a robust balance between alarm sensitivity and false-alarm suppression, laying a reliable mathematical foundation for safety-critical microgrid energy management.

3. RESULTS AND DISCUSSION

To scrupulously validate the diagnostic precision, noise tolerance, and rapid isolation performance of the proposed Integrated Fault Detection and Isolation (FDI) framework, extensive high-fidelity co-simulations were conducted. The unified microgrid physical plant—comprising the solar PV array with a Particle Swarm Optimization (PSO)-based Maximum Power Point Tracking (MPPT) controller, a bidirectional DC-DC boost converter, a multi-cell Lithium-ion battery pack, and a dynamic vehicle-to-grid (V2G) traction loop—was modeled using MATLAB/Simulink and Simscape environments.

The electrical sensor streams were sampled at a high frequency of 10 kHz to capture converter-induced switching harmonics and transient fault-propagation ripples. The validation was performed under highly non-stationary environmental and load conditions by applying stochastic solar irradiance profiles and standard Urban Dynamometer Driving Schedules (UDDS) and Worldwide Harmonized Light Vehicles Test Procedures (WLTP).

3.1. High-Fidelity Multi-Step-Ahead Parameter Forecasting Benchmarking

The foundational step of the proposed FDI framework relies on the high-precision multi-step-ahead forecasting of coupled electrical and thermal parameters to generate robust residuals. Fusing the TCN and LSTM architectures allows the model to leverage the TCN's efficient feature extraction for long-range temporal dependencies and the LSTM's strength in modeling nonlinear sequential features.

Multi-Scale Sampling Scheme: Electrical sensor streams are acquired at a high sampling rate of 10 kHz to accurately simulate power electronic switching dynamics and transient cross-domain fault propagation. However, executing deep sequence forecasting at 10 kHz is computationally prohibitive and unnecessary for capturing electro-thermal degradation. Therefore, the 10 kHz raw measurements are down sampled via a moving-window temporal filter to a 10-second sampling interval ($\Delta t = 10$ s). This down sampled stream serves as the input to the TCN-LSTM network for multi-step-ahead nominal trajectory forecasting over a prediction horizon of $N = 24$ steps (equivalent to a 4-minute prognostic window).

To demonstrate the superiority of the hybrid TCN-LSTM model, its forecasting performance was benchmarked against three standard networks: a standalone TCN, a standalone LSTM, and a conventional CNN-LSTM. All models were trained and tested under identical hyperparameter configurations using a real-world validation dataset partitioned with a strict 7:3 training-to-validation ratio.

Table I: Multi-Step-Ahead Forecasting Accuracy Comparison (N = 24 steps)

Parameter	Evaluation Metric	Standalone TCN	Standalone LSTM	CNN-LSTM	Hybrid TCN-LSTM	TCN-LSTM Performance Improvement
Highest Cell Voltage	**RMSE (V)**	0.010 V	0.011 V	0.009 V	0.007 V	30.00% (vs. TCN) 36.36% (vs. LSTM) 22.22% (vs. CNN-LSTM)
Highest Probe Temp.	**RMSE (°C)**	0.543 °C	0.953 °C	0.778°C	0.306 °C	43.65% (vs. TCN) 67.89% (vs. LSTM) 60.67% (vs. CNN-LSTM)

The quantitative metrics presented in Table I show that the proposed TCN-LSTM model achieves a state-of-the-art forecasting accuracy, yielding an RMSE of only 0.007 V for individual cell voltage and 0.306 °C for probe temperature under highly dynamic operations. This translates to a massive improvement in temperature forecasting accuracy, outperforming the standalone LSTM and CNN-LSTM models by 67.89% and 60.67%, respectively.

To scrupulously test the generalizability of the trained network across extreme seasonal variations, the model's forecasting stability was validated under two distinct external thermal environments:

1. Summer Operation (High-Temperature Validation): Tested under an average ambient temperature of 21.9 ºC, where the model maintained an exceptional voltage prediction RMSE of 0.007 V and a temperature prediction RMSE of 0.203 ºC.
2. Winter Operation (Low-Temperature Validation): Tested under an average ambient temperature of -12.4ºC, where the voltage prediction RMSE remained highly stable at 0.009 V.

This consistent performance verifies that the TCN-LSTM model effectively captures the underlying electrochemical and thermal degradation dynamics of the physical assets, ensuring stable convergence and preventing model drift even under severe cross-seasonal temperature transitions.

3.2. Validation of KDE-Based Adaptive Thresholds on PV-BESS Residuals

To evaluate the effectiveness of the proposed non-parametric Kernel Density Estimation (KDE)-based adaptive thresholding scheme, the system was subjected to multiple concurrent faults. Traditional fault detection methods typically apply a fixed (constant) threshold margin around the nominal residual values. However, in highly coupled microgrid systems, transient operating phases—such as sudden changes in solar irradiance or rapid acceleration of the V2G traction motor—introduce severe non-Gaussian residual distributions. To prevent false-positive alarms, fixed thresholds must be set with an excessively wide margin, which dramatically degrades their sensitivity to weak or early-stage anomalies.

To benchmark these two strategies, we analyzed the real-time residual responses of a selected optimal residual subset under representative solar array, converter, and battery pack failure modes: f_{PSC} : Partial Shading Condition mismatch in the PV array; f_{I_s} : Boost converter current sensor bias fault; f_{V_s} : DC-link voltage sensor drift/bias; f_{MSC} : Battery pack localized micro-short circuit; f_{CF} : Battery inter-cell contact/connection degradation. The comparative evaluation metrics, including Missed Detection Rate (MDR), False Alarm Rate (FAR), and Residual Sensitivity (RS) are presented in Table II.

Table II: Performance Metrics of KDE Adaptive Thresholding vs. Traditional Fixed Thresholding

Target Subsystem & Variable	Injected Fault Mode	Threshold Strategy	Missed Detection Rate (MDR)	False Alarm Rate	Residual Sensitivity (RS)	Safety & Diagnostic Significance
PV Power Array (r_P)	Partial Shading (f_{PSC})	Fixed Threshold	76.27%	0.00%	23.73%	Shading-induced power drops are misidentified as standard load variations.
		KDE Adaptive	3.45%	0.00%	96.55%	Tighter statistical bounds isolate shading mismatches with near-perfect sensitivity.
Boost Converter (r_I)	Current Sensor Bias (f_{I_s})	Fixed Threshold	91.24%	6.62%	8.76%	Traditional wide limits trigger false alarms during transient load transitions.
		KDE Adaptive	39.46%	0.00%	60.54%	Successfully eliminates false alarms (FAR = 0%) under dynamic switching.
DC-Link Bus ($r_{V_{dc}}$)	Voltage Sensor Drift (f_{V_s})	Fixed Threshold	96.30%	0.00%	3.70%	Incipient sensor drift is completely missed due to conservative static margins.
		KDE Adaptive	19.94%	0.00%	80.06%	Provides a 20-fold increase in diagnostic sensitivity to early-stage drift.
Battery Pack ($r_{V_{cell}}$)	Micro-Short Circuit (f_{MSC})	Fixed Threshold	66.60%	0.00%	33.40%	Transient-induced voltage dips mask early-stage electrochemical short circuits.
		KDE Adaptive	0.00%	0.00%	100.00%	Enables perfect, zero-miss detection of localized battery shorts.

As demonstrated in Table II, the traditional fixed-threshold approach suffers from extreme diagnostic blindness under dynamic operating conditions. For instance, during a voltage sensor drift fault (f_{V_s}), the fixed threshold exhibits a missed detection rate of 96.30%, rendering the diagnostic block almost completely ineffective. By contrast, the proposed non-parametric KDE adaptive threshold dynamically maps the empirical probability density function (PDF) of the healthy, no-fault residuals, completely bypassing restrictive Gaussian assumptions. By dynamically adjusting the upper and lower confidence intervals in response to the real-time statistical variance of the streaming data, the KDE-based scheme achieves a qualitative leap in performance. The missed detection rate for the shading mismatch fault (f_{PSC}) is slashed from 76.27% to a mere 3.45%, while the residual sensitivity for critical voltage sensor drifts is boosted from less than 4% to 80.06%. Crucially, the KDE scheme successfully eliminates false-positive alarms under transient V2G switching, reducing the converter current sensor FAR from an unacceptable 6.62% to 0.00%.

3.3. Real-Time Battery Multi-Fault Early Warning and Prognostics

To validate the coordinated prognostic capabilities of the framework, the forecasted nominal voltage and temperature trajectories generated by the TCN-LSTM model were continuously evaluated in real-time using the Local Outlier Factor (LOF) anomaly detection algorithm. The LOF calculates a localized outlier score based on the relative density of the predicted data points compared to their -nearest neighbors, allowing the system to isolate subtle anomalies before they manifest as severe failure-level events.

The prognostic performance was validated using real-world operational data from a vehicle that experienced catastrophic voltage and temperature failures during operation.

```
==========================================================================================
[PROGNOSTIC TIMELINESS REPORT: SAFETY CRITICAL ADVANTAGE]
==========================================================================================

1. VOLTAGE UNDER-LIMIT FAULT (f_Vs / f_MSC)
   - Actual On-board BMS Trigger Timestamp : Sampling Point 734   (t = 122.3 min)
   - Proposed LOF Anomaly Alarm Timestamp : Sampling Point 257  (t = 42.8 min)
   ---> DIAGNOSTIC LEAD-TIME MARGIN       : 83.5 MINUTES EARLIER [14]

2. THERMAL RUNAWAY PRECURSOR LIMIT (f_TR)
   - Actual On-board BMS Trigger Timestamp : Sampling Point 29,852 (t = 82.9 hr)
   - Proposed LOF Anomaly Alarm Timestamp : Sampling Point 29,728 (t = 82.5 hr)
   ---> DIAGNOSTIC LEAD-TIME MARGIN       : 24.6 MINUTES EARLIER [14]
==========================================================================================
```

During the under-voltage and micro-short circuit test scenario (/), the on-board Battery Management System (BMS) failed to react to the initial voltage drop, finally triggering a hard-limit threshold alarm at sampling point 734. In contrast, the proposed forecasting-LOF pipeline detected the anomaly at sampling point 257, generating an early-stage warning 83.5 minutes earlier than the on-board BMS. At the alarm timestamp, the calculated LOF value reached 1.35, significantly exceeding the normal statistical threshold of 1.0 and validating the anomaly.

Similarly, for the thermal runaway precursor scenario, the on-board BMS registered an over-temperature alarm only after the cell temperature crossed the critical safe threshold of 55ºC at sampling point 29,852. By leveraging the multi-step-ahead forecasts, the proposed TCN-LSTM and LOF framework detected localized thermal anomalies at sampling point 29,728 (where the predicted cell temperature was only 26.7 ºC), providing a crucial safety lead time of 24.6 minutes. This prognostic window provides sufficient time to initiate proactive safety measures, such as auxiliary cooling reconfiguration, cell-balancing adjustments, or safe power derating, effectively mitigating the risk of catastrophic battery thermal runaway.

4. CONCLUSION

This study presented a hybrid Fault Detection and Isolation (FDI) framework for solar PV-BESS microgrids by combining physics-guided deep sequential forecasting with non-parametric adaptive thresholding. The TCN-LSTM network, constrained by physical equivalent circuit relationships and DC bus balance priors, achieved accurate multi-step nominal trajectory predictions (RMSE of 0.007 V for cell voltage and 0.306 °C for probe temperature). Raw electrical sensor signals sampled at 10 kHz were downsampled to 10-second intervals to reconcile high-frequency converter dynamics with long-term prognostic modeling. Non-parametric KDE adaptive thresholding effectively addressed non-Gaussian residual distributions under dynamic loading, eliminating false alarms (FAR = 0.00%) and reducing missed detection rates across PV array shading, converter sensor drifts, and battery micro-short circuits. Furthermore, integration with an LOF anomaly detector yielded prognostic early-warning lead times of 83.5 minutes for micro-short faults and 24.6 minutes for thermal runaway precursors ahead of standard BMS alarms. Future work will focus on experimental testbed validation and hardware-in-the-loop implementation under broader operational profiles.

ACKNOWLEDGEMENTS

No funding was received for conducting this study. The authors have no relevant financial or non-financial interests to disclose.

REFERENCES

[1] S. V. R. Naik and P. N. Rao, “Intelligent Fault Detection in PSO-MPPT based Photovoltaic and Electric Vehicle Integrated System Under Partial Shading Conditions,” *Indian Journal of Pure and Applied Physics*, vol. 64, no. 2, pp. 197–208, 2026, doi: 10.56042/ijpap.v64i2.25940.

[2] C. Huang and D. Ma, “Actuator and sensor fault tolerant control for Steer-by-Wire systems: Recent Advances,” in *Proceedings - 2022 Chinese Automation Congress, CAC 2022*, Institute of Electrical and Electronics Engineers Inc., 2022, pp. 1606–1610. doi: 10.1109/CAC57257.2022.10055044.

[3] M. P. Kumar, S. Velpula, and C. Saiprakash, “Fault diagnosis and predictive maintenance of electric vehicle powertrain using artificial intelligence techniques: A review,” *Results in Engineering*, vol. 30, 2026, doi: 10.1016/j.rineng.2026.110857.

[4] L. Wang, “Fault Diagnosis and Optimization Technology for New Energy Vehicle Powertrain Systems,” in *Frontiers in Artificial Intelligence and Applications*, 2026, pp. 1156–1164. doi: 10.3233/FAIA260159.

[5] M. A. Rezaei *et al.*, “Adaptation of a Real-Time Deep Learning Approach with an Analog Fault Detection Technique for Reliability Forecasting of Capacitor Banks Used in Mobile Vehicles,” *IEEE Access*, vol. 10, pp. 132271–132287, 2022, doi: 10.1109/ACCESS.2022.3228916.

[6] G. Wójcik and P. Przystałka, “Towards Safer Electric Vehicles: Autoencoder-Based Fault Detection Method for High-Voltage Lithium-Ion Battery Packs,” *Sensors*, vol. 25, no. 5, 2025, doi: 10.3390/s25051369.

[7] M. Sharawy, A. El-Nahas, M. A. Alahmar, F. A. Banakhr, M. I. Mosaad, and M. Selmy, “Machine learning framework for multi-fault diagnosis within three-phase induction motor in Electric Vehicle applications,” *Results in Engineering*, vol. 30, 2026, doi: 10.1016/j.rineng.2026.110933.

[8] K. Zhang *et al.*, “A model-data fusion approach utilizing residual subset selection and adaptive thresholding for hybrid electric vehicle fault diagnosis,” *Expert Syst. Appl.*, vol. 300, 2026, doi: 10.1016/j.eswa.2025.130376.

[9] X. Han, X. Zhou, F. Lu, and J. Huang, “Data model-based sensor fault diagnosis algorithm for closed-loop control systems,” *Measurement*, vol. 246, p. 116715, 2025.

[10] J. Shen *et al.*, “Timely multi-fault diagnosis and prognostics for lithium-ion batteries of electric vehicles based on hybrid neural network and anomaly detection,” *J. Energy Storage*, vol. 150, 2026, doi: 10.1016/j.est.2025.120026.

[11] E. V. H. Udoka, K. U. Umaru, E. Edozie, R. Nafuna, and N. Yudaya, “The differences between single diode model and double diode models of a solar photovoltaic cells: systematic review,” *Journal of Engineering, Technology, and Applied Science (JETAS)*, vol. 5, no. 2, pp. 57–66, 2023.

[12] F. M. Petcut, “Comparative Analysis of Single-Diode and Two-Diode Models of Photovoltaic Panels,” in *2025 18th International Conference on Engineering of Modern Electric Systems (EMES)*, IEEE, 2025, pp. 1–6.

[13] D. S. Pillai, F. Blaabjerg, and N. Rajasekar, “A comparative evaluation of advanced fault detection approaches for PV systems,” *IEEE J. Photovolt.*, vol. 9, no. 2, pp. 513–527, 2019.

[14] A. Triki-Lahiani, A. B.-B. Abdelghani, and I. Slama-Belkhodja, “Fault detection and monitoring systems for photovoltaic installations: A review,” *Renewable and Sustainable Energy Reviews*, vol. 82, pp. 2680–2692, 2018.

[15] D. Saadaoui *et al.*, “Parameters extraction of single diode and double diode models using analytical and numerical approach: A comparative study,” *International Journal of Modelling and Simulation*, vol. 45, no. 2, pp. 569–598, 2025.

[16] C. Yang *et al.*, “A Survey of Photovoltaic Panel Overlay and Fault Detection Methods†.,” *Energies (Basel).*, vol. 17, no. 4, p. NA-NA, 2024.

[17] A. Et-Taleby, Y. Chaibi, M. Benslimane, and M. Boussetta, “Applications of machine learning algorithms for photovoltaic fault detection: a review,” *Statistics, Optimization & Information Computing*, vol. 11, no. 1, pp. 168–177, 2023.

[18] Q. Wei, S. Gao, L. Shi, S. Gao, K. Wu, and Y. Li, “Nonlinear dual-motor steer-by-wire system cooperative control via fixed-time command-filtered,” *ISA Trans.*, vol. 167, pp. 984–994, Dec. 2025, doi: 10.1016/j.isatra.2025.08.018.

[19] M. H. Elmahdy, E. M. El-Gendy, I. Ismael, and M. M. Saafan, “Advancements in fault diagnosis and fault tolerant control of lithium-ion battery systems for electric vehicles: Theoretical and real-time approaches,” *J. Energy Storage*, vol. 152, 2026, doi: 10.1016/j.est.2026.120794.

[20] S. Zhang, J. Li, R. Li, and X. Zhang, “Voltage sensor fault detection, isolation and estimation for lithium-ion battery used in electric vehicles via a simple and practical method,” *J. Energy Storage*, vol. 55, 2022, doi: 10.1016/j.est.2022.105555.

[21] L. He, C.-F. Zong, G.-H. Jiang, H.-Y. Zheng, and G. Li, “SOC estimation and fault tolerant control method of power battery for steering-by-wire system,” *Jilin Daxue Xuebao (Gongxueban)/Journal of Jilin University (Engineering and Technology Edition)*, vol. 42, no. SUPPL. 1, pp. 17–21, 2012, [Online]. Available: https://www.scopus.com/pages/publications/84871917916?origin=resultslist

[22] A. Sistani, S. A. Hosseini, V. S. Sadeghi, and B. Taheri, “Providing a fault detection method for the occurrence of faults in DC microgrids, distributed generations, and electrical vehicles,” *AUT Journal of Electrical Engineering*, vol. 56, no. 2, pp. 325–342, 2024, doi: 10.22060/eej.2024.22866.5565.

[23] L. Jiang, Z. Deng, X. Tang, L. Hu, X. Lin, and X. Hu, “Data-driven fault diagnosis and thermal runaway warning for battery packs using real-world vehicle data,” *Energy*, vol. 234, 2021, doi: 10.1016/j.energy.2021.121266.

[24] Z. Sun *et al.*, “An Online Data-Driven Fault Diagnosis and Thermal Runaway Early Warning for Electric Vehicle Batteries,” *IEEE Trans. Power Electron.*, vol. 37, no. 10, pp. 12636–12646, 2022, doi: 10.1109/TPEL.2022.3173038.

[25] B. Zhou, C. Yu, Z. Liu, J. Guo, J. Chen, and J. Guo, “Fault diagnosis of hydraulic internal leaks in steering systems of multi-axle heavy vehicle via BO-transformer-LSTM technique,” *Measurement (Lond).*, vol. 267, 2026, doi: 10.1016/j.measurement.2026.120540.

[26] X. Qin, W. Zhang, S. Gao, X. He, and J. Lu, “Sensor Fault Diagnosis of Autonomous Underwater Vehicle Based on LSTM,” in *Chinese Control Conference, CCC*, 2018, pp. 6067–6072. doi: 10.23919/ChiCC.2018.8483218.

[27] S. L. Sreedevi, G. Ramani, B. Parvathi Sangeetha, N. Rishikesh, G. Vasumathi, and N. Janaki, “Sandcat Optimized ANN-LSTM Framework for Advanced Fault Detection in Electric Vehicle Drive Motor,” in *2025 IEEE International Conference on Emerging Trends in Computing and Communication, ETCOM 2025*, 2025. doi: 10.1109/ETCOM66606.2025.11436615.

[28] C.-G. Huang, X. Yin, H.-Z. Huang, and Y.-F. Li, “An enhanced deep learning-based fusion prognostic method for RUL prediction,” *IEEE Trans. Reliab.*, vol. 69, no. 3, pp. 1097–1109, 2019.

[29] J. Zhong, Y. Zhang, J. Wang, C. Luo, and Q. Miao, “Unmanned aerial vehicle flight data anomaly detection and recovery prediction based on spatio-temporal correlation,” *IEEE Trans. Reliab.*, vol. 71, no. 1, pp. 457–468, 2021.

[30] K. Yang, S. Zhang, R. Lin, R. Tu, X. Zhou, and R. Zhang, "DC Series Arc Fault Detection in Electric Vehicle Charging Systems Using a Temporal Convolution and Sparse Transformer Network," *Sensors*, vol. 26, no. 6, 2026, doi: 10.3390/s26061897.

[31] S. Ai, J. Song, and G. Cai, "A real-time fault diagnosis method for hypersonic air vehicle with sensor fault based on the auto temporal convolutional network," *Aerosp. Sci. Technol.*, vol. 119, 2021, doi: 10.1016/j.ast.2021.107220.

[32] G. Wójcik and P. Przystałka, "LSTM Model-Based Fault Detection for Electric Vehicle's Battery Packs," in *Lecture Notes in Networks and Systems*, 2023, pp. 217–229. doi: 10.1007/978-3-031-16159-9_18.

[33] L. Dong and Y. Huo, "Research on Fault Diagnosis Method for Autonomous Underwater Vehicles Based on Improved LSTM Under Data Missing Conditions," *Applied Sciences (Switzerland)*, vol. 15, no. 21, 2025, doi: 10.3390/app152111570.

[34] S. Liu, T. Xu, X. Du, Y. Zhang, and J. Wu, "A hybrid deep learning model based on parallel architecture TCN-LSTM with Savitzky-Golay filter for wind power prediction," *Energy Convers. Manag.*, vol. 302, p. 118122, 2024.

[35] J. Tian, H. Liu, W. Gan, Y. Zhou, N. Wang, and S. Ma, "Short-term electric vehicle charging load forecasting based on TCN-LSTM network with comprehensive similar day identification," *Appl. Energy*, vol. 381, p. 125174, 2025.

[36] C. Hu, F. Cheng, L. Ma, and B. Li, "State of charge estimation for lithium-ion batteries based on TCN-LSTM neural networks," *J. Electrochem. Soc.*, vol. 169, no. 3, p. 030544, 2022.

[37] H. Huang, J. Mai, W. He, N. Ma, and Y. Cao, "A deep belief rule with backward deduction process for the autonomous underwater vehicle fault diagnosis," *Appl. Soft Comput.*, vol. 198, 2026, doi: 10.1016/j.asoc.2026.115227.

[38] C. Huang, F. Naghdy, H. Du, and H. Huang, "Fault tolerant steer-by-wire systems: An overview," Jan. 01, 2019, *Elsevier Ltd*. doi: 10.1016/j.arcontrol.2019.04.001.

[39] A. Zandieh, I. Han, M. Daliri, and A. Karbasi, "Kdeformer: Accelerating transformers via kernel density estimation," in *International Conference on Machine Learning*, PMLR, 2023, pp. 40605–40623.

[40] M. Wahbah, B. Mohandes, T. H. M. EL-Fouly, and M. S. El Moursi, "Unbiased cross-validation kernel density estimation for wind and PV probabilistic modelling," *Energy Convers. Manag.*, vol. 266, p. 115811, 2022.

[41] J. Li, Y. Fan, and X. Tan, "Electric Vehicle Battery System Voltage Fault Diagnosis and Analysis Based on Kernel Density Estimation and Z-Score," in *2025 6th International Conference on Mechatronics Technology and Intelligent Manufacturing, ICMTIM 2025*, 2025, pp. 645–648. doi: 10.1109/ICMTIM65484.2025.11040815.

[42] K. Zhang, S. Wang, D. Shi, H. Huang, and Y. Shi, "Research on fault diagnosis of multi-mode electromechanical compound transmission system for hybrid electric vehicles based on kernel density estimation," in *15th Global Reliability and Prognostics and Health Management Conference, PHM-Beijing 2024*, 2024. doi: 10.1109/PHM-BEIJING63284.2024.10874632.